Films of Gold Nanoparticles and Oleylamine at the Air-Water Interface: the Unexpected Morphological Changes of Gold

Mouktar Nour Mahamoud, Gilles Paboeuf, Bertrand Lefeuvre, Véronique Vié, Fabienne Gauffre

Films of Gold Nanoparticles and Oleylamine at the Air-Water Interface: the Unexpected Morphological Changes of Gold

Mouktar Nour Mahamoud,[a] Gilles Paboeuf,[b] Bertrand Lefeuvre,[a] Véronique Vié*,[b] and Fabienne Gauffre*[a]

a. Univ Rennes, CNRS, ISCR-UMR6226, F-35000 Rennes, France.
b. Univ Rennes, CNRS, IPR-UMR6251, ScanMAT-UAR 2025, F-35000 Rennes, France.

Abstract. We investigated films of gold nanoparticles (AuNPs) stabilized with a weakly interacting ligand (oleylamine, OlA), at the air-water interface. Despite its low purity, commercial OlA is widely used for AuNPs synthesis as it allows to reach a narrow size distribution. This weakly bound ligand equilibrates between the solid-fluid and the air-water interfaces, competing with the nanoparticle to reduce the air-water interfacial energy. We investigated the compression isotherms for various gold/OlA ratios, and the morphology of the film was monitored during compression, using Brewster Angle Microscopy (BAM), Atomic Force Microscopy (AFM) and transmission electron microscopy (TEM). This multiscale analysis reveals that the ligand impurities segregates within the film, forming domains of distinct heights, like a 2D-foam. The AuNPs clusterize within the boundaries between the domains. Most surprisingly, we observe that the particles diameter decreases drastically from ca 13.6 nm to less than 3 nm after deposition at the interface.

Introduction.

The 2D-monolayers and multilayers of plasmonic nanoparticles have many applications such as light harvesting, sensing, SERS spectroscopy and electron transport, due to their enhanced and controllable electromagnetic properties.[1–7] Recently, several approaches based on the interfacial assembly of pre-formed nanoparticles have been reviewed.[8] Among them, the self-assembly at fluid interfaces (either oil-water or air-water is one of the most appealing since compared to solid interfaces, fluid interfaces have the potential to self-correct defaults.[9,10] In particular, Langmuir troughs equipped with mobile barriers enable to tune the interparticle distances at the air-water interface. Then, the transfer of monolayers to solid substrate via the Langmuir-Blodgett technique enables to access to 2D or 3D particle lattices.[11–13] Note also that, nanoparticles pre-formed via solution synthesis are generally of much of higher quality, regarding the control of their size and morphology, than what can currently be achieved via reduction directly at an interface.[14] Besides planar interfaces, particle films also play an important role in emulsions and foams, where they very efficiently limit droplet and bubble coalescence.[15] In particular, it is well recognized that particle-stabilized emulsions (Pickering emulsions) are highly stable, which plays an important role in industrial processes. At a lower scale, nanoparticles were shown to stabilize submicronic droplets in Ouzo emulsions,[16,17] while at a larger scale, particles of several tens of micrometers form strong coatings at the surface of macroscopic droplets in air, forming the so-called “liquid marbles”.[18,19] Studying particles at interfaces can provide useful information about their surface energy and wettability, properties which are extremely difficult to determine otherwise.[20] However, he physics underlying interparticle interactions, stability and self-

assembly at interfaces is much more complex and less well understood than in bulk and has been the subject of increasing attention.[21]

Inorganic nanoparticles are often regarded as hard spheres. However, hydrophobic nanoparticles such as these used to generate Langmuir monolayers, present an organic coating, generally of alkyl chain ligands or of hydrophobic polymers, which lowers their wettability with water.[20,22,23] These ligands are also useful in the synthesis to obtain a well-controlled size distribution and may also be tailored to provide additional functionalities to the nanoparticles.[24–29] Depending on their binding energy with the nanoparticle, the ligand may be involved in a more or less rapid dynamical exchange between the nanoparticle surface and is environment.[30,31] Tools to study dynamical ligand exchanges remains limited, and only a few examples are reported, using NMR in bulk suspensions of nanoparticles.[30,31] However, investigation of particles with weakly interacting ligands at interfaces are still lacking.

Among the many ligands used for nanoparticle synthesis, oleylamine (OlA) has played a specific role, either alone or in combination with oleic acid.[32] It is often used together as a solvent, a reducing agent and a protecting ligand. Indeed, oleylamine readily gives up electrons at high temperatures. It is also liquid over a large range of temperatures without decomposition (20-360°C), allowing high temperature synthesis as well as easy recovery.[33] Synthesis of gold nanoparticles in pure OlA yield relatively narrow distributions of size, with a good reproducibility. Depending on the experimental conditions, the size of the particles is usually of 12-13 nm which is appropriate for applications involving plasmon coupling. After the synthesis, the relatively weak bond formed between amines and gold enables ligand exchange or access to the surface for catalysis. As an example, the adsorption energy of methylamine on gold surface is -0.3 eV, to be compared with -1.85 eV for methyl thiol.[34] As a consequence of this weak interaction, an excess of alkylamines is required to stabilize the nanoparticles against aggregation. However, experiments achieved in the case of strong binding ligands such as alkylthiols have shown that excess free ligand, even in small proportion, has important effects on the film mechanics and morphology, by increasing the compressibility of the film and easing multilayer formation.[11,35,36] To date, there is a lack of information about films of alkylamine-stabilized gold nanoparticles, and more generally about composites films of nanoparticles and alkyl ligands.

In this article, we investigate the film properties of gold nanoparticles stabilized with oleylamine at the air-water interface. The particles were prepared by the hot reduction of a gold salt in pure oleylamine. With the aim to investigate the effect of varying the ratio nanoparticle/ligand, we submitted the particles to several steps of centrifugation followed by redispersion in a solution of known concentration of OlA. The compression isotherms were built using a Langmuir trough equipped with mobile barriers and a Wilhelmy balance. Large scale organization and phase changes within the film were monitored by Brewster Angle Microscopy. The morphology of the film was also investigated at the micrometer to nanometer scale using AFM and TEM.

Results and discussion

Synthesis and characterization of the gold nanoparticles. We used commercial oleylamine (*cis*-9-octadecenoic amine, *cis*-$CH_3(CH_2)_7CHCH(CH_2)_8NH_2$, OlA) of technical grade (70% purity), as it is unexpensive and widely used for nanoparticle synthesis.[32,37–39] The predominant impurities oleylamine is a *trans* isomer (up to 43%). Shorter chains and/or less saturated impurities are also found, as well as oxidated derivatives of amines (amides and nitroalkanes).[33] The AuNP were synthesized by a rapid injection of the gold precursor in hot oleylamine (150°C) under argon atmosphere[40]. The AuNPs were separated from the reaction media by centrifugation after addition of ethanol, to recover a pellet that could be suspended in the desired solvent. The obtained particles exhibit a mean size of 13.6 nm with

a standard deviation of 1.5 nm (Figure 1). Assuming that the AuNPs are in compact organization in areas showing hexagonal tiling, we measured a mean interparticle distance in "close contact" of 3.0 $\pm$ 0.3 nm. This distance is lower than twice the length of the oleylamine chain (2 x 2.05 nm, see SI), suggesting that the chains interpenetrates. This is consistent with the bend conformation of the oleylamine chains around its insaturation, which prevents the formation of a dense amine coating around the particles, as reported previously.[41]

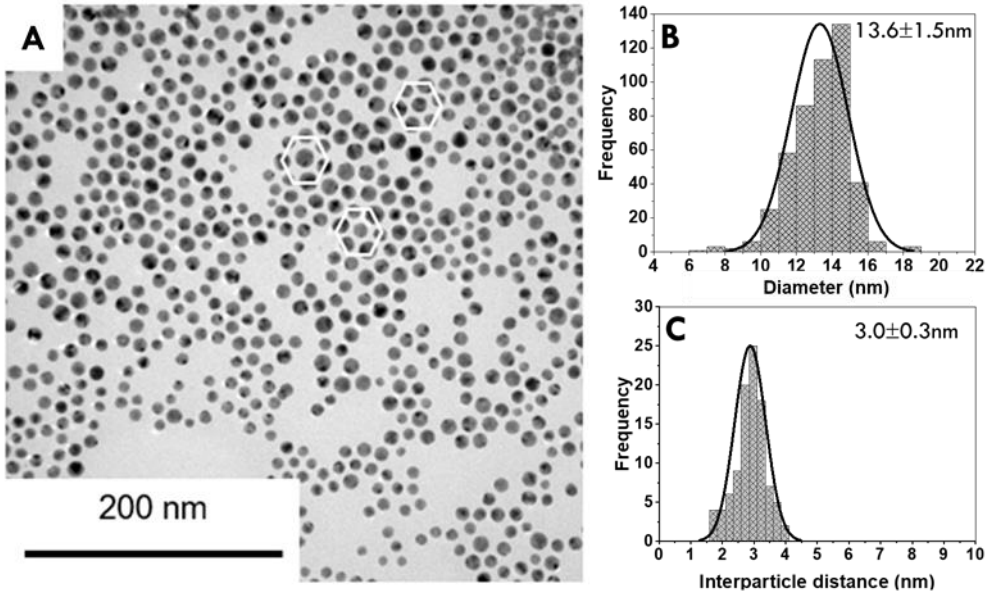

Figure 1 : TEM analysis of the gold nanoparticles synthesized in oleylamine. (a) TEM image of the AuNPs from THF suspension. The white hexagons exemplify the close packing of the OlA-stabilized AuNps, where minimal interparticle distance can be measured. (b) Size distribution of the AuNps with Gaussian fit. (c) Distribution of the interparticle distances measured in close-packed areas. Mean size (or interparticle distance) and standard deviations are indicated on graphs.

Choice of the spreading solvent and concentration. As mentioned previously, several groups reported a lack of reproducibility when investigating interfacial films containing nanoparticles.[35,36] In an effort to identify the sources of discrepancies, we investigated both the effect of the nature of the solvent and of the initial concentration of the spreading suspension. In a first series of experiments, we selected dichloromethane, as fast evaporating and poorly water-miscible solvents are generally preferred to spread films at the air-water interfaces. Thus, the pellet of AuNP was dispersed in dichloromethane and the resulting suspension spread at the air-water interface in a Langmuir through equipped with mobile barriers. Interestingly, images of the film observed using Brewster Angle Microscopy revealed needle-like aggregates with a characteristic length of roughly 35 µm (Figure 2a, see also Figure SI. 2 for a typical compression isotherm and more BAM images). A second series of experiments run with THF as the spreading solvent exhibited very different morphologies, since only isotropic aggregates were observed (Figure 2b). The TEM analysis of a dichloromethane suspension of the AuNPs revealed large particles of uneven shapes most probably resulting from coalescence of the AuNPs (Figure 2a, inset). In contrast, in THF the morphology of the particles evolves only marginally over several weeks. In the following, we use only THF as the spreading solvent. We do not have a clear explanation for the different stability of these AuNPs in THF vs dichloromethane. In particular, these

two solvents have very similar solvation properties, as evidenced by their Hansen parameters (see ESI).[42,43]

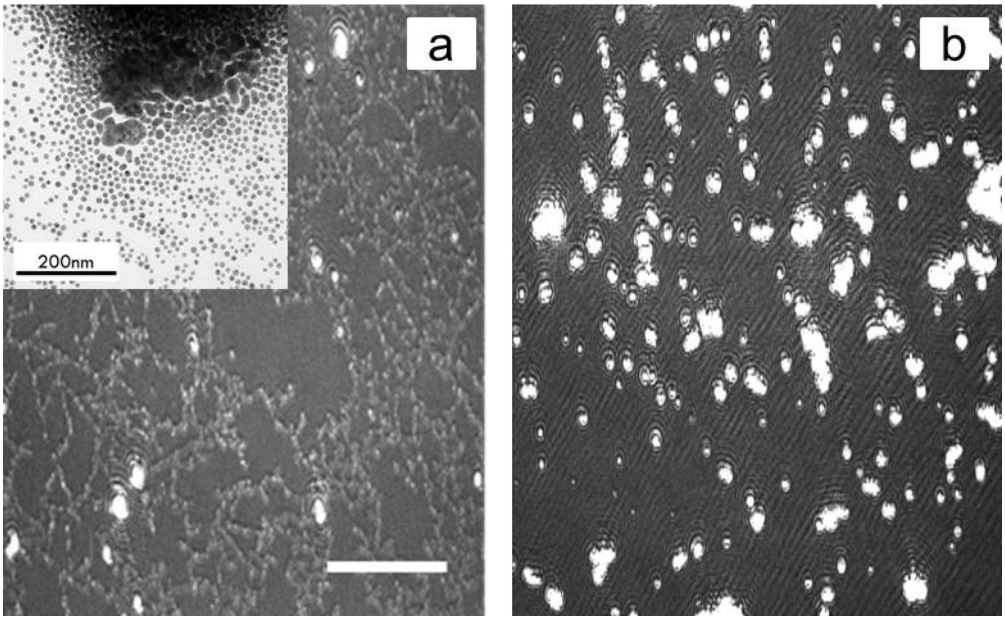

Figure 2 : Effect of the spreading solvent on the morphologies of OlA-stabilized gold nanoparticles, as observed by BAM. (a) spreading solvent: dichloromethane; Inset: TEM of the AuNPs freshly dispersed in dichloromethane.; (b) spreading solvent: THF. Size of BAM images: 400 x 500 µm, scale: 1µm).

We also hypothesized that the concentration of the spreading suspension could have an effect on the morphology of the film, since OlA is in dynamic equilibrium between the particle surface and the liquid phase. To investigate this effect, we investigated the behavior of films made from three suspensions, obtained by dilution 5, 10 and 20 times of the same mother suspension. The gold concentration in the mother suspension was estimated by ICP at 300 mg/L. Figure SI. 3 shows the three isotherms (i.e. surface pressure vs molecular area) obtained by compressing the films with the mobile barriers. The exact concentration in OlA being unknown, the x axis represents the normalized molecular area ($A.f_d/V$, in arbitrary units,) where A is the area of the trough, f_d the dilution factor and V the deposited volume. Clearly, all three isotherms fuse nicely on a same curve, showing that the dilution up to 20 times does not destabilize the system. Note that Langmuir isotherms of conventional amphiphilic molecules generally show the following sequences when compressed from large molecular areas. They first pass through a highly compressible gaseous phase shown as a horizontal line in the isotherm. Then, transitions to one or more less compressible phase (often called “liquid expanded”) can be observed. Finally, the system reaches a regime of very low compressibility in which the amphiphilic molecules are closely packed.[44]

Effect of the OlA/AuNP ratio. We recall here that these AuNPs are synthesized in the presence of a very large excess of oleylamine, which prevents aggregation. If the ligand is washed up by cycles of centrifugation and redispersion into THF, the particles aggregate irreversibly after 4 cycles. To avoid aggregation, we washed the particles several time using an OlA solution of known concentration, using THF as the solvent (see the Material and methods section for details). The minimal concentration that allowed us to stabilize the AuNPs (up to 9 cycles of centrifugation/redispersion) was found to be approximately $4.5\ 10^{-3}$ mole/L. Assuming a molecular area of 20 $Å^2$ for OlA, we find that the amount of amine necessary to stabilize the AuNPs can cover more than 750 times the total nanoparticle surface (see SI for details of calculation).

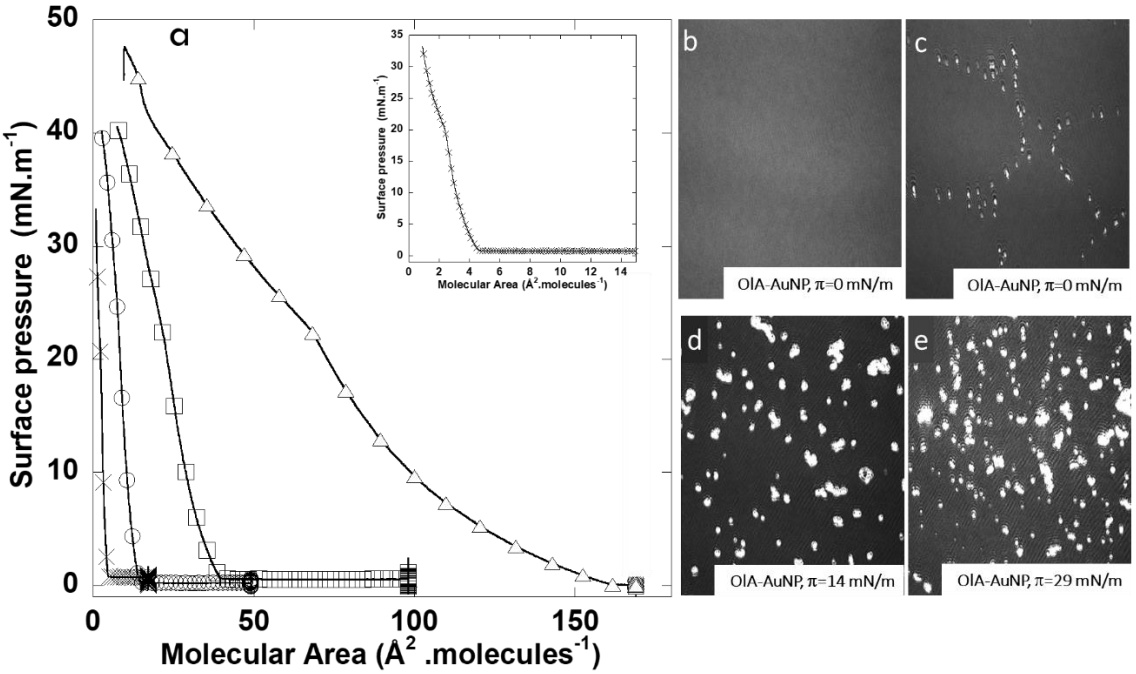

Figure 3 a) Compression isotherms of oleylamine and oleylamine-stabilized gold nanoparticles, with various molar ratio of gold over oleylamine. (x) [Au]/[OlA] = 0 ; (o) [Au]/[OlA] = 1.2.10^{-3}; (□) 2.25.10^{-3} ; (Δ) 6.7.10^{-3}. The x axis represents the surface divided by the number of oleylamine molecules. (b-e) BAM images (400 x 500 µm) of films of oleylamine stabilized gold nanoparticles at the air water interface at different stages before and during compression. Measured pressure as indicated on images. [Au]/[OlA] = 1.2.10^{-3}.

Using this method to reduce and control the concentration of OlA, we investigated the effect of the amount of gold nanoparticles on the compressibility of the films. Figure 3 shows the compression isotherms of OlA, and of three suspensions of OlA-stabilized AuNPs with different molar ratio of gold to OlA. The x-axis represents the film area divided by the number of deposited surfactant molecules. Consequently, the discrepancy between the isotherms should result only from the presence of AuNPs. Note that to calculate the number of deposited OlA molecules, we made the crude assumption that the commercial product contains only OlA. The isotherm obtained for the sample without AuNPs is reproduced in the inset Figure 3, with an extended scale. For films made of a single amphiphilic molecule, the lift-off of pressure ($\pi > 0$) generally allows to estimate the surface area occupied by one molecule at the air-water interface. Here, lift-off occurs at 4.6 Å^2/molecule, which is by far smaller than what is expected for OlA (from 20 to 36 Å^2/molecule, see ESI section 1). This suggests that a significant amount of OlA is dragged into the subphase, most probably driven by the solubility of the spreading solvent (THF) with water. This apparent molecular area increases with the particle loading, to 15.3, 39.1, and finally 158.3 Å^2/molecule for [Au]/[OlA] = 1.2.10^{-3}; (□) 2.25.10^{-3}; (Δ) 6.7.10^{-3} respectively. Taking a look at the slope of the isotherms, which correspond to the inverse of the compressibility of the film, it is also clear that the presence of the particles strongly increases the compressibility. Finally, a tilt in the slope is observed at a pressure of $\pi = 20$mN.m^{-1}, for all isotherms. This change of compressibility regime is usually associated to conformational change of spread molecules as observed for saturated phospholipids.[45,46] Note here that the presence of particles reduces the available air-water interface for the surfactant molecules. This is consistent with the pressure lift-off at higher areas, but cannot account for the higher compressibility. Thus, at this stage we do not have a clear hypothesis to explain these seemingly contradictory observations. To enlighten the behavior of the composite Ola-AuNPs films, we investigated their morphology and more specifically the organization of the AuNPs within the film, using complementary imaging techniques operating at different scales.

Multiscale analysis of the film morphology (BAM, AFM and TEM) We first used Brewster Angle Microscopy (BAM) to characterize the films at large scale,[47] at different stages before and after compression. We first investigated the case of OlA films, i.e. in the absence of the nanoparticles (Figure SI. 4). In this case, the deposited film looks homogeneous before compression (Figure SI. 4a) and randomly distributed aggregates are observed at π =25 mN.m^{-1} (Figure SI. 4 b). When OlA-stabilized AuNPs are spread on the surface (Figure 3b-e), we can clearly observe the formation of a cellular structure with a characteristic length of about 250 µm (Figure 3c). The separating walls exhibit bright spots, that most probably correspond to aggregates of gold nanoparticles. As more suspension is spread on the surface, the spots grow in size, while remaining confined between the cells. Note that these aggregates are not present in the initial solution nor in the early stage of deposition as Figure 3b shows a homogeneous interface. This cellular structure most probably results from the segregation of different molecular species contained in the commercial OlA into separate domains, leading to a confinement of the AuNPs into the cell walls and their aggregation. Indeed, as mentioned before, alkylamines interact only weakly with AuNPs and the local environment of the particles at the air water interface can be radically different from that in solution. Furthermore, the building of a percolating network of cell walls, rigidified by aggregates of AuNps explains why interfacial pressure arises at much larger surface area in the presence of the AuNPs. Upon lateral compression, aggregates grow further but the cellular structure is rapidly lost (Figure 3d&e). This is consistent with the relatively high compressibility of the AuNP containing films after pressure lift-off.

To generalize this study, and show its relevance to commercial nanoparticles, we also investigated the case of commercial quantum dots (QD, in the present case luminescent Cadmium Selenide/Zinc Sulfide core/shell Nanoparticles), stabilized by oleic acid (see section 6 in ESI). Oleic acid molecules interact with the zinc sulfide surface through a relatively strongly bidentate coordination of oleic acid as a carboxylate to Zn^{2+}.[48] However, the presence of free oleic acid molecules and/or amphiphilic impurities is also probable. Also in this case BAM imaging evidences a cellular structure at low pressure, with the QD confined within the walls (Figure SI. 5). The cell structure is lost upon compression, and a dense percolating network of particles is formed.

In order to investigate the morphology of the film and the organization of the AuNPs within the film at the microscopic level, we sampled films using the Langmuir-Blodgett method for atomic force microscopy (AFM) analysis. Figure 4 presents images of AuNPs containing films after transfer on solid substrate for [Au]/[OlA] = 1.2.10^{-3}. The films were sampled at two different surface pressures: π = 15 mN.m^{-1} (Figure 4a-c) and π = 30 mN.m^{-1} (Figure 4d), i.e. below and beyond the liquid expanded/condensed phase transition (see the corresponding isotherm in Figure SI. 6).

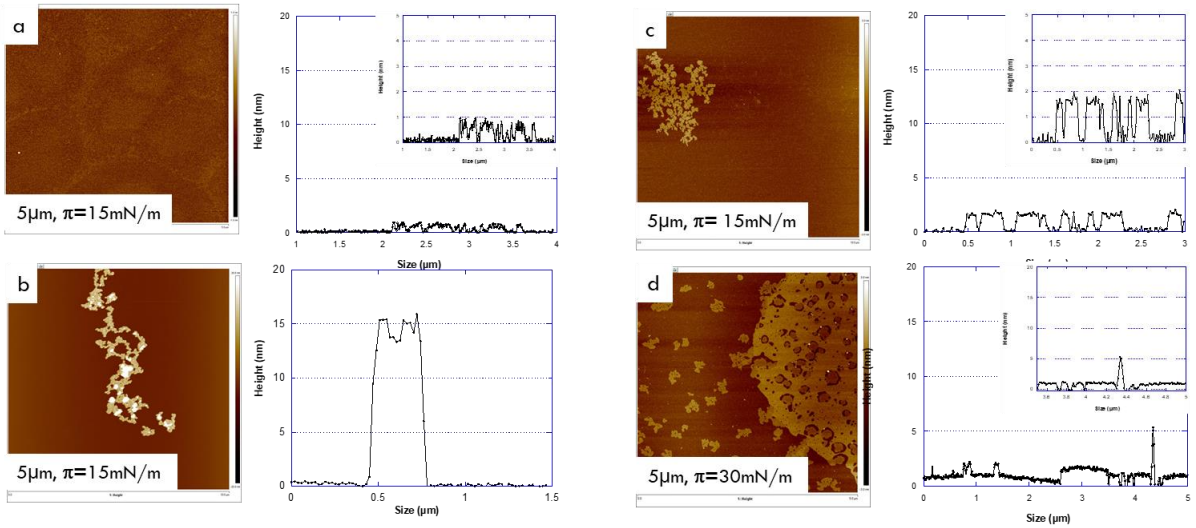

Figure 4 : AFM image and profile analysis of oleylamine-stabilized AuNP films collected at the air/water interface by the Langmuir-Blodgett technique. The film ([Au]/[OlA] = 1.2 10^{-3}) was transferred either at pressure π = 15 mN.m^{-1} or π = 30 mN.m^{-1}. Image size: 5µmx5µm.

The AFM observations revealed contrasted areas thorough the film, which can be classified in three types (Figure 4). (1) The background (Figure 4a) is characterized by very small height variations (less than 1 nm). The presence of cellular patterns and patches of slightly different heights may be related to those observed by BAM before compression. It confirms the molecular segregation, possibly of the trans isomer of oleylamine (elaidylamine) present in high concentrations in commercial oleylamine.[33] Indeed, trans isomers experience much higher attractive interactions and close packing than their cis counter parts.[49] They also adopt a more extended conformation. Therefore, patches of elaidylamine are expected to outstrip from the background.[45] (2) A few aggregates with height over the background of the order of 15 nm (Figure 4b). (3) Numerous fractal aggregates with a typical height over the background in between 0.8 and 1.5 nm. These aggregates densify and become wider as the surface pressure is increased (Figure 4c, π = 15 mN.m^{-1} and Figure 4d π = 30 mN.m^{-1}). While the aggregates of height of 10 nm most probably correspond to the pristine AuNPs, we were intrigued at this stage by the numerous aggregates of intermediate height (typically 2 nm) observed in Figure 4c&d. Therefore, we also sampled the same film on TEM grids to image specifically the organization of the gold nanoparticles. To this aim, samples of the interfacial film were collected directly over TEM grid at the air-water interface at π = 30 mN.m^{-1}.

Figure 5 shows TEM analysis of a sample taken at a random location over the film, at the end of a compression experiment. It evidences numerous gold particles of diameter less than 3 nm, with an angular shape. A careful visual observation of the film also enables samplings in areas with higher reflectivity. In this case, TEM analysis shows particles with sizes apparently similar to the pristine particles. However, a closer investigation of the size distribution reveals also a decrease of the mean size (Figure SI. 7) from 12.6 $\pm$ 4.2 nm before spreading to 10.5 $\pm$ 4.8 nm within the film. An analysis of the interparticle distances was also achieved, revealing a rapprochement of the particles from <d> = 2.9 $\pm$ 0.7 nm before spreading to <d> = 1.5 $\pm$ 0.6 nm after spreading.

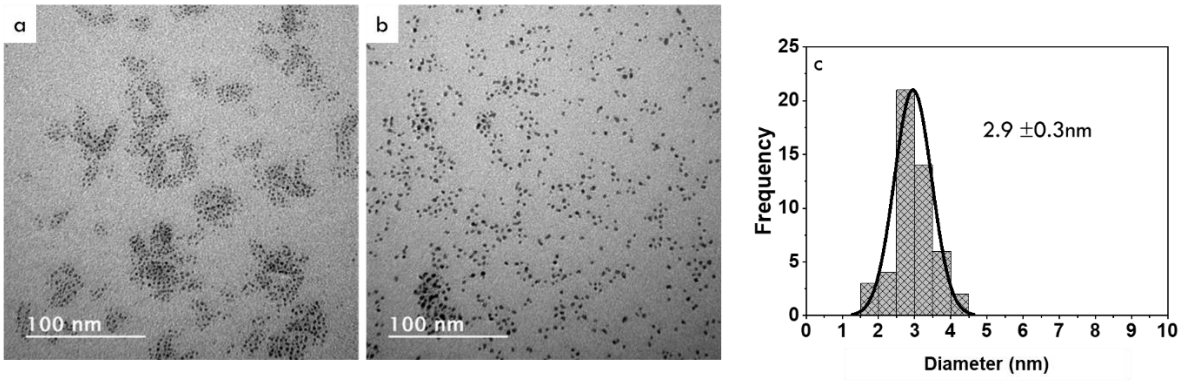

Figure 5 : (a-b) TEM images of ultrasmall particles collected on a TEM grid sampled randomly over a film of oleylamine-stabilized gold nanoparticles ([Au]/[OlA] = 1.2 10^{-3}) at the air-water interface, at the end of the compression procedure.(c) Size histogram.

Such a decrease in size of the nanoparticles was very unexpected and at the present time we do not have a clear explanation for this phenomenon. Searching the literature, we found only two reports of a change of size (increase) of gold nanoparticles within a film.[50,51] However, redistribution of gold atoms between gold particles is largely described in bulk, in the context of "digestive ripening" (also called reverse Ostwald ripening"), under conditions of excess ligand and intensive heating. [52–55] The driving force for digestive ripening is the affinity between the ligand and the particle. This favors a total increase of the solid surface and leads to a smaller average diameter. In general, the final mean size lays in between both larger and smaller particles that are present in the initial system, and the dispersity is lowered. This is the result of etching at the atomic scale and redistribution of the atoms between particles. Heating helps overcome the energy barrier to remove gold atoms from the particle. However, breaking of large particles to form very small nanocrystals at room temperature was also observed.[55] Breaking is due to the presence of crystalline defects, such as twinning boundaries. Coming back to our study, the AuNPs do show crystalline defects as can be observed Figure 1. At the air water interface, the environment of the gold nanoparticles changes drastically in comparison to the spreading suspension and particularly they experience a high local concentration of OlA or associated amphiphilic impurities. In addition, bare gold being very hydrophilic to slightly hydrophobic,[56] it is reasonable to assume that OlA desorbs from the immersed particle surface. Finally, breaking of the AuNPs into ~3nm nanocrystals at the air-water interface could be driven by favorable amine-gold interactions and facilitated by microstresses in their structure. The arrangement of the small nanocrystals into larger patches as shown Figure 5a supports the hypothesis of larger particles breaking up into small ones. Finally, the morphological changes of the particles during the course of the compression experiment, could also explain the unusual shape of the compression isotherms.

Conclusion.

We have investigated films of oleylamine-stabilized gold nanoparticles at the air-water interface by combining interfacial pressure measurements (compression isotherms) and structural analyses at different scales (TEM, AFM and BAM). We intentionally worked with commercial oleylamine of low purity (70%), which is commonly used in the synthesis of gold nanoparticles. To achieve reproducible conditions, we controlled the amount of ligand by an appropriate centrifugation procedure. We show that an excess surface (ca 750 times) of oleylamine is necessary to prevent aggregation during

centrifugation, which is a consequence of the weak binding of oleylamine to gold. Even at very low particle loading, the behavior of the compression isotherms (π-A) of these composite interfacial films cannot be explained within the standard framework of films of amphiphilic molecules. We have shown that the segregation of the film components leads to a cellular structure, with particles aggregating inside the walls of this 2D foam. The same structure is observed for commercial quantum dots stabilized with oleic acid. Very surprisingly, we also observed a spectacular reduction in the size of the gold nanoparticles, from an initial 13 nm to 3 nm. This unexpected result should provide an impetus to study the morphological changes of nanoparticles within interfacial film of ligands in more details.

Materials and methods.

Materials. Tetrahydrofuran (THF, inhibitor-free, HPLC grade, ≥99.9 %), Oleylamine (>70%), dichloromethane (5anhydrous, ≥99.8%°, contains 40-150 ppm amylene as stabilizer), Ethanol (96%) were purchased from Sigma-Aldrich. Samples were made using MilliQ water (18.2 MΩ.cm−1). The hydrophobic Cadmium Selenide/Zinc Sulfide (CdSe/ZnS) core/shell quantum dots (QD) stabilized with oleic acid (emission at 665 nm) were purchased from Cytodiagnostic.

Synthesis of gold nanoparticles: 5 mL of oleylamine (OlA) is first degassed in vacuo, then heated to 150°C in a Schlenk under argon atmosphere. Subsequently, 5 mL OlA containing 125.5 mg $HAuCl_4$, $3H_2O$ (0.64 mmol) is introduced into the OlA at 150°C. The mixture was then kept at this temperature with magnetic stirring for 1h30. Initially pale orange in color, the mixture gradually turns pink and then intense red. Heating is then stopped and the mixture is left to stir until it returns to room temperature. After cooling, 5 mL ethanol is added to precipitate the gold nanoparticles (AuNPs). The mixture is then distributed into 13 tubes and centrifuged at 11700 g for 5 minutes (using a MIKRO 220R centrifuge, Hettich). The upper phases were removed and the pellets were stored. Then, depending on the experiment, different solvents (THF or dichloromethane) were used to disperse the particles. To adjust OlA to a desired concentration, the particles were first dispersed in 1 mL of THF and then centrifugated at 11700 g for 30 minutes. Then 0.8 mL of the supernatant was removed and replaced by the same volume of a OlA solution at the target concentration. This last operation was repeated two more times.

Nanoparticle Characterization:

TEM. Transmission electron microscopy analysis was achieved using a JEOL 2100 LaB_6 microscope equipped with a GATAN Orius 200D camera (THEMIS, Scanmat). A minimum of 600 particles was counted to build the histograms, either manually of using an automated procedure with Image-J software.

Gold titration by ICP-EOS. Au concentration was determined using an iCAP 7000 Series ICP-OES spectrometer (Thermo Scientific) under argon flow, previously calibrated from 0 to 2 ppm Au. Sample solution was placed in open plastic vials and dried under the fume hood. Then the gold material was soaked for 2 days in 1 mL nitric acid and then completed to 25 mL with milliQ water. A value of 10 % uncertainty was estimated over ICP measurements, by digesting and titrating three differents alicots of the same mother suspension.

Compression isotherms. The isotherms were performed using Langmuir troughs equipped by two mobile barriers (Nima Technology, UK) able to compress the interfacial film with a controlled rate. The size of the trough was 700 cm^2 (10*70cm^2). The surface pressure (Pi, $mN.m^{-1}$) is measured using the Wilhelmy method, using a filter paper plate connected to a microelectronic feedback system (Nima Technology, UK). The surface pressure measurement accuracy is 0.5 $mN.m^{-1}$. Before all experiments,

the cleanliness of the interface was ensured by measuring ultrapure water for 5 minutes and under compression. The experiments were conducted as follows: the solution was spread to the interface with a Hamilton syringe of 100µL, drop by drop (~1µL). The time deposition was depending of the concentration or nature of solution. Indeed, to improve a good isotherm reproducibility, the initial conditions should correspond at a minimization of interactions between particles or molecules. In others words, the molecules should be in gaseous phase and in this case, the surface pressure is equal to zero. After deposition, 20 min stay is allowed for solvent evaporation and reorganization of molecules or particles. Then, the interface was compressed by moving the barriers (5 mm/min) and surface pressure was recorded as a function of the time and of the area. The curves presented in this study are representative of at least two experiments. The temperature was maintained constant at 21.5+-0.5°C.

BAM. Micrometric scale visualization of the air-liquid interface was achieved with Brewster angle microscopy (BAM), using a Nanofilm EP3 microscope (Accurion, DE), as previously described.[57] A 532 nm laser beam, reflected by the interface at the Brewster angle, was captured by a 10× objective and CCD detector. The Brewster angle is determined by the Fresnel equation with values typically around 53.1°. At this angle, p-polarized light is perfectly transmitted through the interface without reflection, resulting in minimal light intensity on pure water. However, when particles or molecules cover the interface, the refractive index differs from water, thus grayscale variations are observed, depending on the density at the interface. The trough of 97.5 cm² (19.5*5 cm²) was used equipped by surface pressure sensors (Small trough – KVS Biolin) and mobile barriers. The Langmuir films were prepared, and isotherms recorded in the same way as described above. Images are 500*400 µm². The temperature was maintained constant at 21.5 $\pm$ 0.5°C.

AFM. Atomic force microscopy (AFM) was used to observe the organization of interfacial films at a nanometric scale, as previously described.[58] The interfacial film was transferred to a mica plate using the Langmuir-Blodgett method and imaged by AFM (Multimode Nanoscope 8, Bruker, France) in PeakForce Quantitative Nanomechanical Mapping (QNM) mode in air. Topographic images were taken at different scale. All images were taken using a standard silicon cantilever (SNL-10, Bruker, France) with a stiffness of 0.3 $N.m^{-1}$, a scan rate of 1 Hz, and an image resolution of 512×512 pixels. Analysis of the AFM images was carried out using Gwyddion software (version 2.55).

Acknowledgements. This work was supported by the French National Agency of Research (ANR-20-CE06-0031-01 OUZOFAN). We also acknowledge the financial support of the University of Rennes and of the CNRS. The authors also wish to thank L. Rault (Thémis- ScanMAT UAR 2025), for electron microscopy.

References

(1) Yogev, D.; Efrima, S. Novel Silver Metal Liquidlike Films. *J. Phys. Chem.* **1988**, *92* (20), 5754–5760. https://doi.org/10.1021/j100331a041.

(2) Zhao, M.; Wang, X.; Liang, Z.; Zhang, B.; Liao, Y.; He, Y.; Ma, Y. Plasmonic Array at the Liquid–Liquid Interface: A Dual-Mode Optical Sensing Platform for Multianalytes. *Anal. Chem.* **2022**, acs.analchem.2c03996. https://doi.org/10.1021/acs.analchem.2c03996.

(3) Ye, Z.; Li, C.; Chen, Q.; Xu, Y.; Bell, S. E. J. Self-Assembly of Colloidal Nanoparticles into 2D Arrays at Water–Oil Interfaces: Rational Construction of Stable SERS Substrates with Accessible Enhancing Surfaces and Tailored Plasmonic Response. *Nanoscale* **2021**, *13* (12), 5937–5953. https://doi.org/10.1039/D0NR08803J.

(4) Shipway, A. N.; Katz, E.; Willner, I. Nanoparticle Arrays on Surfaces for Electronic, Optical, and Sensor Applications. *ChemPhysChem* **2000**, *1* (1), 18–52. https://doi.org/10.1002/1439-7641(20000804)1:1<18::AID-CPHC18>3.0.CO;2-L.

(5) Brust, M.; Bethell, D.; Kiely, C. J.; Schiffrin, D. J. Self-Assembled Gold Nanoparticle Thin Films with Nonmetallic Optical and Electronic Properties. *Langmuir* **1998**, *14* (19), 5425–5429. https://doi.org/10.1021/la980557g.
(6) Joseph, Y.; Besnard, I.; Rosenberger, M.; Guse, B.; Nothofer, H.-G.; Wessels, J. M.; Wild, U.; Knop-Gericke, A.; Su, D.; Schlögl, R.; Yasuda, A.; Vossmeyer, T. Self-Assembled Gold Nanoparticle/Alkanedithiol Films: Preparation, Electron Microscopy, XPS-Analysis, Charge Transport, and Vapor-Sensing Properties. *J. Phys. Chem. B* **2003**, *107* (30), 7406–7413. https://doi.org/10.1021/jp030439o.
(7) Huang, Y.; Dai, L.; Song, L.; Zhang, L.; Rong, Y.; Zhang, J.; Nie, Z.; Chen, T. Engineering Gold Nanoparticles in Compass Shape with Broadly Tunable Plasmon Resonances and High-Performance SERS. *ACS Appl. Mater. Interfaces* **2016**, *8* (41), 27949–27955. https://doi.org/10.1021/acsami.6b05258.
(8) Song, L.; Huang, Y.; Nie, Z.; Chen, T. Macroscopic Two-Dimensional Monolayer Films of Gold Nanoparticles: Fabrication Strategies, Surface Engineering and Functional Applications. *Nanoscale* **2020**, *12* (14), 7433–7460. https://doi.org/10.1039/C9NR09420B.
(9) Turek, V. A.; Cecchini, M. P.; Paget, J.; Kucernak, A. R.; Kornyshev, A. A.; Edel, J. B. Plasmonic Ruler at the Liquid–Liquid Interface. *ACS Nano* **2012**, *6* (9), 7789–7799. https://doi.org/10.1021/nn302941k.
(10) Velleman, L.; Sikdar, D.; Turek, V. A.; Kucernak, A. R.; Roser, S. J.; Kornyshev, A. A.; Edel, J. B. Tuneable 2D Self-Assembly of Plasmonic Nanoparticles at Liquid|liquid Interfaces. *Nanoscale* **2016**, *8* (46), 19229–19241. https://doi.org/10.1039/C6NR05081F.
(11) Swierczewski, M.; Bürgi, T. Langmuir and Langmuir–Blodgett Films of Gold and Silver Nanoparticles. *Langmuir* **2023**, *39* (6), 2135–2151. https://doi.org/10.1021/acs.langmuir.2c02715.
(12) Zhu, Y.; Deng, W.; Chen, L.; Courtois, J.; Tian, Q.; Zhang, X.; Almásy, L.; Yan, M.; Xiong, K. Langmuir-Blodgett-Assembled Monolayer Zinc Ferrite Nanoparticle Film with Unique Photogenerated Charge Carrier Separation Efficiency and Charge Transfer Behavior. *Applied Surface Science* **2020**, *534*, 147646. https://doi.org/10.1016/j.apsusc.2020.147646.
(13) Acharya, S.; Hill, J. P.; Ariga, K. Soft Langmuir–Blodgett Technique for Hard Nanomaterials. *Advanced Materials* **2009**, *21* (29), 2959–2981. https://doi.org/10.1002/adma.200802648.
(14) Gazil, O.; Virgilio, N.; Gauffre, F. Synthesis of Ultrasmall Metal Nanoparticles and Continuous Shells at the Liquid/Liquid Interface in Ouzo Emulsions. *Nanoscale* **2022**, *14* (37), 13514–13519. https://doi.org/10.1039/D2NR04019K.
(15) Kim, H.-J.; Lee, C.-R.; Park, D.-G.; Chang, J. W.; Lee, H.-Y. Study of the Adsorption Behaviors of Amphiphilic Gold Nanoparticles at the Liquid–Liquid Interface Dependent on Surface Properties. *J. Phys. Chem. C* **2020**, *124* (30), 16423–16430. https://doi.org/10.1021/acs.jpcc.0c03760.
(16) Goubault, C.; Iglicki, D.; Swain, R. A.; McVey, B. F. P.; Lefeuvre, B.; Rault, L.; Nayral, C.; Delpech, F.; Kahn, M. L.; Chevance, S.; Gauffre, F. Effect of Nanoparticles on Spontaneous Ouzo Emulsification. *Journal of Colloid and Interface Science* **2021**, *603*, 572–581. https://doi.org/10.1016/j.jcis.2021.06.104.
(17) Gazil, O.; Rault, L.; Iglicki, D.; Collière, V.; Karacaoglan, G.; Poinsot, D.; Bouzid, M.; Hierso, J.-C.; Kahn, M. L.; Virgilio, N.; Gauffre, F. Spontaneous Emulsification of Organometallic Complexes Applied to the Synthesis of Nanocapsules Active for H_2 Release from Ammonia-Borane. *Langmuir* **2024**, *40* (32), 16824–16832. https://doi.org/10.1021/acs.langmuir.4c01307.
(18) Aussillous, P.; Quéré, David. Liquid Marbles. *Nature Communications* **2001**, *411*, 924–927.
(19) Arbatan, T.; Li, L.; Tian, J.; Shen, W. Liquid Marbles as Micro-Bioreactors for Rapid Blood Typing. *Advanced Healthcare Materials* **2012**, *1* (1), 80–83. https://doi.org/10.1002/adhm.201100016.
(20) Santini, E.; Krägel, J.; Ravera, F.; Liggieri, L.; Miller, R. Study of the Monolayer Structure and Wettability Properties of Silica Nanoparticles and CTAB Using the Langmuir Trough Technique. *Colloids and Surfaces A: Physicochemical and Engineering Aspects* **2011**, *382* (1–3), 186–191. https://doi.org/10.1016/j.colsurfa.2010.11.042.

(21) Bresme, F.; Oettel, M. Nanoparticles at Fluid Interfaces. *J. Phys.: Condens. Matter* **2007**, *19* (41), 413101. https://doi.org/10.1088/0953-8984/19/41/413101.
(22) Garbin, V.; Crocker, J. C.; Stebe, K. J. Nanoparticles at Fluid Interfaces: Exploiting Capping Ligands to Control Adsorption, Stability and Dynamics. *Journal of Colloid and Interface Science* **2012**, *387* (1), 1–11. https://doi.org/10.1016/j.jcis.2012.07.047.
(23) Horozov, T. S.; Binks, B. P.; Aveyard, R.; Clint, J. H. Effect of Particle Hydrophobicity on the Formation and Collapse of Fumed Silica Particle Monolayers at the Oil–Water Interface. *Colloids and Surfaces A: Physicochemical and Engineering Aspects* **2006**, *282–283*, 377–386. https://doi.org/10.1016/j.colsurfa.2005.11.085.
(24) Heuer-Jungemann, A.; Feliu, N.; Bakaimi, I.; Hamaly, M.; Alkilany, A.; Chakraborty, I.; Masood, A.; Casula, M. F.; Kostopoulou, A.; Oh, E.; Susumu, K.; Stewart, M. H.; Medintz, I. L.; Stratakis, E.; Parak, W. J.; Kanaras, A. G. The Role of Ligands in the Chemical Synthesis and Applications of Inorganic Nanoparticles. *Chem. Rev.* **2019**, *119* (8), 4819–4880. https://doi.org/10.1021/acs.chemrev.8b00733.
(25) Mahato, K.; Nagpal, S.; Shah, M. A.; Srivastava, A.; Maurya, P. K.; Roy, S.; Jaiswal, A.; Singh, R.; Chandra, P. Gold Nanoparticle Surface Engineering Strategies and Their Applications in Biomedicine and Diagnostics. *3 Biotech* **2019**, *9* (2), 57. https://doi.org/10.1007/s13205-019-1577-z.
(26) Spataro, G.; Dazzazi, A.; Fortuny, S.; Champouret, Y.; Coppel, Y.; Rubio-Garcia, J.; Bouhaouss, A.; Gauffre, F.; Kahn, M. L. Insight into the Role of Ligands in the Yellow Luminescence of Zinc Oxide Nanocrystals. *Eur. J. Inorg. Chem.* **2016**, *2016* (13–14), 2056–2062. https://doi.org/10.1002/ejic.201501186.
(27) Zhang, Y.; Clapp, A. Overview of Stabilizing Ligands for Biocompatible Quantum Dot Nanocrystals. *Sensors* **2011**, *11* (12), 11036–11055. https://doi.org/10.3390/s111211036.
(28) Guan, H.; Harris, C.; Sun, S. Metal–Ligand Interactions and Their Roles in Controlling Nanoparticle Formation and Functions. *Acc. Chem. Res.* **2023**, *56* (12), 1591–1601. https://doi.org/10.1021/acs.accounts.3c00156.
(29) Calvin, J. J.; Brewer, A. S.; Alivisatos, A. P. The Role of Organic Ligand Shell Structures in Colloidal Nanocrystal Synthesis. *Nat Synth* **2022**, *1* (2), 127–137. https://doi.org/10.1038/s44160-022-00025-4.
(30) Coppel, Y.; Spataro, G.; Pagès, C.; Chaudret, B.; Maisonnat, A.; Kahn, M. L. Full Characterization of Colloidal Solutions of Long-Alkyl-Chain-Amine-Stabilized ZnO Nanoparticles by NMR Spectroscopy: Surface State, Equilibria, and Affinity. *Chemistry – A European Journal* **2012**, *18* (17), 5384–5393. https://doi.org/10.1002/chem.201102050.
(31) Wolff, N.; Beuck, C.; Schaller, T.; Epple, M. Possibilities and Limitations of Solution-State NMR Spectroscopy to Analyze the Ligand Shell of Ultrasmall Metal Nanoparticles. *Nanoscale Adv.* **2024**, *6* (13), 3285–3298. https://doi.org/10.1039/D4NA00139G.
(32) Mourdikoudis, S.; Liz-Marzán, L. M. Oleylamine in Nanoparticle Synthesis. *Chem. Mater.* **2013**, *25* (9), 1465–1476. https://doi.org/10.1021/cm4000476.
(33) Baranov, D.; Lynch, M. J.; Curtis, A. C.; Carollo, A. R.; Douglass, C. R.; Mateo-Tejada, A. M.; Jonas, D. M. Purification of Oleylamine for Materials Synthesis and Spectroscopic Diagnostics for *Trans* Isomers. *Chem. Mater.* **2019**, *31* (4), 1223–1230. https://doi.org/10.1021/acs.chemmater.8b04198.
(34) Hoft, R. C.; Ford, M. J.; McDonagh, A. M.; Cortie, M. B. Adsorption of Amine Compounds on the Au(111) Surface: A Density Functional Study. *J. Phys. Chem. C* **2007**, *111* (37), 13886–13891. https://doi.org/10.1021/jp072494t.
(35) Griesemer, S. D.; You, S. S.; Kanjanaboos, P.; Calabro, M.; Jaeger, H. M.; Rice, S. A.; Lin, B. The Role of Ligands in the Mechanical Properties of Langmuir Nanoparticle Films. *Soft Matter* **2017**, *13* (17), 3125–3133. https://doi.org/10.1039/C7SM00319F.
(36) Comeau, K. D.; Meli, M. V. Effect of Alkanethiol Chain Length on Gold Nanoparticle Monolayers at the Air–Water Interface. *Langmuir* **2012**, *28* (1), 377–381. https://doi.org/10.1021/la202895n.

(37) He, M.; Protesescu, L.; Caputo, R.; Krumeich, F.; Kovalenko, M. V. A General Synthesis Strategy for Monodisperse Metallic and Metalloid Nanoparticles (In, Ga, Bi, Sb, Zn, Cu, Sn, and Their Alloys) via in Situ Formed Metal Long-Chain Amides. *Chem. Mater.* **2015**, *27* (2), 635–647. https://doi.org/10.1021/cm5045144.
(38) Pesesse, A.; Carenco, S. Influence of the Copper Precursor on the Catalytic Transformation of Oleylamine during Cu Nanoparticle Synthesis. *Catal. Sci. Technol.* **2021**, *11* (15), 5310–5320. https://doi.org/10.1039/D1CY00639H.
(39) Liu, X.; Atwater, M.; Wang, J.; Dai, Q.; Zou, J.; Brennan, J. P.; Huo, Q. A Study on Gold Nanoparticle Synthesis Using Oleylamine as Both Reducing Agent and Protecting Ligand. *J. Nanosci. Nanotech.* **2007**, *7* (9), 3126–3133. https://doi.org/10.1166/jnn.2007.805.
(40) Liu, S.; Chen, G.; Prasad, P. N.; Swihart, M. T. Synthesis of Monodisperse Au, Ag, and Au–Ag Alloy Nanoparticles with Tunable Size and Surface Plasmon Resonance Frequency. *Chem. Mater.* **2011**, *23* (18), 4098–4101. https://doi.org/10.1021/cm201343k.
(41) Borges, J.; Ribeiro, J. A.; Pereira, E. M.; Carreira, C. A.; Pereira, C. M.; Silva, F. Preparation and Characterization of DNA Films Using Oleylamine Modified Au Surfaces. *Journal of Colloid and Interface Science* **2011**, *358* (2), 626–634. https://doi.org/10.1016/j.jcis.2011.03.039.
(42) Gårdebjer, S.; Andersson, M.; Engström, J.; Restorp, P.; Persson, M.; Larsson, A. Using Hansen Solubility Parameters to Predict the Dispersion of Nano-Particles in Polymeric Films. *Polym. Chem.* **2016**, *7* (9), 1756–1764. https://doi.org/10.1039/C5PY01935D.
(43) Saita, S.; Takeda, S.; Kawasaki, H. Hansen Solubility Parameter Analysis on Dispersion of Oleylamine-Capped Silver Nanoinks and Their Sintered Film Morphology. *Nanomaterials* **2022**, *12* (12), 2004. https://doi.org/10.3390/nano12122004.
(44) Vollhardt, D. Effect of Unsaturation in Fatty Acids on the Main Characteristics of Langmuir Monolayers. *J. Phys. Chem. C* **2007**, *111* (18), 6805–6812. https://doi.org/10.1021/jp0704822.
(45) Vié, V.; Van Mau, N.; Lesniewska, E.; Goudonnet, J. P.; Heitz, F.; Le Grimellec, C. Distribution of Ganglioside G_{M1} between Two-Component, Two-Phase Phosphatidylcholine Monolayers. *Langmuir* **1998**, *14* (16), 4574–4583. https://doi.org/10.1021/la980203p.
(46) Bourlieu, C.; Paboeuf, G.; Chever, S.; Pezennec, S.; Cavalier, J.-F.; Guyomarc'h, F.; Deglaire, A.; Bouhallab, S.; Dupont, D.; Carrière, F.; Vié, V. Adsorption of Gastric Lipase onto Multicomponent Model Lipid Monolayers with Phase Separation. *Colloids and Surfaces B: Biointerfaces* **2016**, *143*, 97–106. https://doi.org/10.1016/j.colsurfb.2016.03.032.
(47) De Mul, M. N. G.; Mann, J. A. Determination of the Thickness and Optical Properties of a Langmuir Film from the Domain Morphology by Brewster Angle Microscopy. *Langmuir* **1998**, *14* (9), 2455–2466. https://doi.org/10.1021/la9713154.
(48) Granados-Oliveros, G.; Pineros, B. S. G.; Calderon, F. G. O. CdSe/ZnS Quantum Dots Capped with Oleic Acid and L-Glutathione: Structural Properties and Application in Detection of Hg2+. *Journal of Molecular Structure* **2022**, *1254*, 132293. https://doi.org/10.1016/j.molstruc.2021.132293.
(49) Iimura, K.; Yamauchi, Y.; Tsuchiya, Y.; Kato, T.; Suzuki, M. Two-Dimensional Dendritic Growth of Condensed Phase Domains in Spread Monolayers of Cis-Unsaturated Fatty Acids. *Langmuir* **2001**, *17* (15), 4602–4609. https://doi.org/10.1021/la010236w.
(50) Swami, A.; Kumar, A.; Selvakannan, P.; Mandal, S.; Sastry, M. Langmuir–Blodgett Films of Laurylamine-Modified Hydrophobic Gold Nanoparticles Organized at the Air–Water Interface. *Journal of Colloid and Interface Science* **2003**, *260* (2), 367–373. https://doi.org/10.1016/S0021-9797(03)00047-X.
(51) Pei, L.; Mori, K.; Adachi, M. Investigation on Arrangement and Fusion Behaviors of Gold Nanoparticles at the Air/Water Interface. *Colloids and Surfaces A: Physicochemical and Engineering Aspects* **2006**, *281* (1–3), 44–50. https://doi.org/10.1016/j.colsurfa.2006.02.029.
(52) Leff, D. V.; Ohara, P. C.; Heath, J. R.; Gelbart, W. M. Thermodynamic Control of Gold Nanocrystal Size: Experiment and Theory. *J. Phys. Chem.* **1995**, *99* (18), 7036–7041. https://doi.org/10.1021/j100018a041.

(53) Sun, Y.; Jose, D.; Sorensen, C.; Klabunde, K. Alkyl and Aromatic Amines as Digestive Ripening/Size Focusing Agents for Gold Nanoparticles. *Nanomaterials* **2013**, *3* (3), 370–392. https://doi.org/10.3390/nano3030370.
(54) Bhaskar, S. P.; Vijayan, M.; Jagirdar, B. R. Size Modulation of Colloidal Au Nanoparticles via Digestive Ripening in Conjunction with a Solvated Metal Atom Dispersion Method: An Insight Into Mechanism. *J. Phys. Chem. C* **2014**, *118* (31), 18214–18225. https://doi.org/10.1021/jp505121b.
(55) Prasad, B. L. V.; Stoeva, S. I.; Sorensen, C. M.; Klabunde, K. J. Digestive-Ripening Agents for Gold Nanoparticles: Alternatives to Thiols. *Chem. Mater.* **2003**, *15* (4), 935–942. https://doi.org/10.1021/cm0206439.
(56) Cayre, O. J.; Paunov, V. N. Contact Angles of Colloid Silica and Gold Particles at Air−Water and Oil−Water Interfaces Determined with the Gel Trapping Technique. *Langmuir* **2004**, *20* (22), 9594–9599. https://doi.org/10.1021/la0489615.
(57) Derde, M.; Nau, F.; Lechevalier, V.; Guérin-Dubiard, C.; Paboeuf, G.; Jan, S.; Baron, F.; Gautier, M.; Vié, V. Native Lysozyme and Dry-Heated Lysozyme Interactions with Membrane Lipid Monolayers: Lateral Reorganization of LPS Monolayer, Model of the Escherichia Coli Outer Membrane. *Biochimica et Biophysica Acta (BBA) - Biomembranes* **2015**, *1848* (1), 174–183. https://doi.org/10.1016/j.bbamem.2014.10.026.
(58) Kergomard, J.; Carrière, F.; Paboeuf, G.; Chonchon, L.; Barouh, N.; Vié, V.; Bourlieu, C. Interfacial Adsorption and Activity of Pancreatic Lipase-Related Protein 2 onto Heterogeneous Plant Lipid Model Membranes. *Biochimie* **2023**, *215*, 12–23. https://doi.org/10.1016/j.biochi.2023.04.001.

Table of Contents